Efficient and Accurate Methods for Computing the Gravitational Field of Irregular-Shaped Bodies

Hermann Meißenhelter
Institute for Computer Graphics and Virtual Reality
University of Bremen
Bibliothekstraße 5, 28359 Bremen, Germany
meissenhelter@cs.uni-bremen.de

Matthias Noeker
Royal Observatory of Belgium (ROB)
& Université catholique de Louvain (UCLouvain)
Avenue Circulaire 3, 1180 Uccle, Belgium
matthias.noeker@observatory.be

Tom Andert
Institute of Space Technology and Space Applications (ISTA)
Bundeswehr University Munich
Werner-Heisenberg-Weg 39,85577 Munich, Germany
tom.andert@unibw.de

René Weller
Institute for Computer Graphics and Virtual Reality
University of Bremen
Bibliothekstraße 5, 28359 Bremen, Germany
weller@cs.uni-bremen.de

Benjamin Haser
Institute of Space Technology and Space Applications (ISTA)
Bundeswehr University Munich
Werner-Heisenberg-Weg 39,85577 Munich, Germany
benjamin.haser@unibw.de

Özgür Karatekin
Royal Observatory of Belgium (ROB)
Avenue Circulaire 3, 1180 Uccle, Belgium
ozgur.karatekin@observatory.be

Birgit Ritter
Royal Observatory of Belgium (ROB)
Avenue Circulaire 3, 1180 Uccle, Belgium
birgit.ritter@observatory.be

Max Hofacker
Institute of Space Technology and Space Applications (ISTA)
Bundeswehr University Munich
Werner-Heisenberg-Weg 39,85577 Munich, Germany
max.hofacker@unibw.de

Larissa Balestrero Machado
Institute of Space Technology and Space Applications (ISTA)
Bundeswehr University Munich
Werner-Heisenberg-Weg 39,85577 Munich, Germany
larissa.balestrero@unibw.de

Gabriel Zachmann
Institute for Computer Graphics and Virtual Reality
University of Bremen
Bibliothekstraße 5, 28359 Bremen, Germany
zach@cs.uni-bremen.de

***Abstract*—Small bodies (e.g. asteroids and moons) are one of the most important targets for physical exploration of space. For space missions, it is a central aspect to test the guidance, navigation, and control algorithms. This is typically ensured through physically-based simulations of the space mission in a virtual testbed, because of its time and cost-efficiency. Information about the gravitational field is crucial for the orbit and especially for planning a landing maneuver. Most small bodies have an irregular shape, which contributes to a complex gravitational field.**

In this study, we present and compare three different methods to model the gravitational field of small bodies and apply them to three test cases that we describe in detail.

Our first method is based on the polyhedral method that provides a closed-form analytical solution of the gravity field for (assumed) homogeneous density. The idea behind the second method is to represent the small body's mass by a polydisperse sphere packing. This allows us an easy and efficient computation through parallelization on the GPU (Graphics Processing Unit). The third method models the internal mass distribution of the body as a set of solid elements in spherical coordinates. The body is divided into longitudes and latitudes and the radius is divided into subsections. The used size of the volume elements is chosen to ensure high accuracy in representing the shape of the body. All three methods are also applicable on the surface of the body, making it interesting in the context of surface gravimetry.

We evaluate the three methods using two ideal shapes (sphere and cube) and one real shape model (Martian moon Phobos). We compare the gravitational acceleration at their surface and measure the relative error of the models concerning the analytical solutions. We also look at the computational cost of each method. Our proposed methods indicate that each of them is suitable for modeling asteroids with different characteristics. We provide reliable gravitation data for purposes such as spacecraft orbit analysis and evaluation of the small body's surface domain.

978-1-6654-3760-8/22/$31.00 ©2022 IEEE

TABLE OF CONTENTS

1. INTRODUCTION

In the last years, several robotic spacecraft have visited small celestial bodies, i.e. asteroids, and comets. For example, the Japanese Hayabusa mission touched down on the surface of the near-Earth object Itokawa in November 2005 to collect material from the surface [1]. The follow-up Hayabusa-2 mission, launched in 2014, arrived at its target in June 2018 and deployed two rovers and a small lander onto the surface of asteroid Ryugu. After the spacecraft successfully fired an impactor into the asteroid in February 2019 to create an artificial crater a sample was collected from beneath the surface of the asteroid [2]. The spacecraft is now on its way to the small asteroid 1998 KY26 during the extended mission. The comet 67P/Churyumov-Gerasimenko was orbited by the European Rosetta spacecraft from August 2014 until the end of September 2016 including the landing of Rosetta's Philae lander in November 2014. The mission ended with the landing of the Rosetta spacecraft on the comet on 30th September 2016. The spacecraft of the still-active mission OSIRIS-REx traveled to the near-Earth asteroid Bennu and collected a sample of the material from the surface. The sample will return to Earth in 2023. The planetary defense mission Hera[1], which is currently under development at the European Space Agency (ESA), will be launching in October 2024. The spacecraft will visit the 65803 Didymos binary asteroid and will measure among other scientific objectives the outcome of NASA's DART mission kinetic impactor test.

During all of the above-mentioned missions, close-proximity operations have been or will be carried out. The conventional way to model the gravitational attraction acting on a spacecraft uses a spherical harmonic [3] or ellipsoidal harmonics [4] representation for the gravity field. This method is of high accuracy and low computational cost, but with the disadvantage that the spherical harmonic or ellipsoidal harmonics representation is only valid outside of the circumscribing sphere (Brillouin sphere). It diverges inside of the Brillouin sphere, e.g. [5]. Therefore, it cannot be used when a spacecraft or lander is getting close to the surface of an irregularly shaped body and alternative methods are needed for representing and calculating the gravity field inside the Brillouin sphere.

However, when missions include a landing on such a small body, the spacecrafts obviously have to descend into the Brillouin sphere. Moreover, they usually have to land autonomously, due to the communication delay. Consequently, a detailed model of the gravity field inside the Brillouin sphere is essential for successful missions to small bodies. Even though the type of method is a basic prerequisite to model and design the trajectory of a lander on an irregularly shaped body, it can also be used for autonomous landing on a small body concerning the higher computational onboard capabilities. This would also include autonomous detection and selection of the landing site and therefore also the onboard computation of different landing trajectories. Another application of the methods is to model the interior structure of a body based on its known gravity field and shape for example derived from Radio Science and camera observations from larger distances.

Various methods have been proposed to circumvent this handicap of the divergence inside the Brillouin sphere, i.e. to compute the gravitational field closer to the surface. They typically differ significantly for the computation time and accuracy. The next section provides a review of these methods with their advantages and also shortcomings.

In this paper, we propose a method to systematically compare such gravity modelling algorithms. In order to do so, we have defined a set of challenging shapes:

- A perfect sphere. For this shape, we can compute the gravitational field analytically. It is easy and fast to compute, however, a sphere cannot be polygonized perfectly. Hence, we additionally provide polygonal approximations of the sphere in different resolutions and different parametrizations. This is challenging, especially for models that rely on polygonal shape models.
- A perfect cube. Similar to the sphere, we can derive the gravitational field of a cube analytically. In contrast to the sphere, it can be perfectly polygonized. However, due to the sharp edges, it is challenging for methods that do not rely on polygonization.
- A highly detailed polygonal model of the Martian moon Phobos. This case is prototypical for a small celestial body of irregular shape. Moreover, there is currently an active mission that actively measures its gravitational field. This will be improved further by the currently planned upcoming Japanese MMX mission. Hence, in the near future, our results can be directly compared to actual measurements.

We selected three commonly used methods – namely a polyhedral method and two different mascon methods – in order to compare them systematically. In Section 3 we start with a detailed description of the three methods, while the succeeding Section 4 addresses the selected test cases. Section 5 covers and discusses the obtained results via the polyhedral method and the mascon methods for the various shapes (sphere, cube, and the Mars moon Phobos), followed by conclusions and future work.

2. PREVIOUS WORK

In this section, we firstly provide an overview of the different methods used to compute the gravitational field of small bodies. Second, we review earlier work that focused, like this work, on the comparison between these different methods to compute the gravitational field.

Gravitational Field Methods

For the calculation of the gravitational field inside the Brillouin sphere and hence on the body's surface, different methods have been developed. The most accurate method, at least as long as we assume a constant distribution of the density, is the *Polyhedral Method (PM)* [6]. The accuracy depends only on the polygonal resolution of the celestial body's 3D model. A drawback is that it is relatively computationally intensive.

[1] https://www.heramission.space/

The computation time increases with an increasing polygon count. We describe this method in detail in our Section 3 below. There exist some extensions to allow the PM to handle varying densities within the body. The sliver approach developed by [7] does this on a global level. Variations on the local scale surrounding individual evaluation points were presented by [8]. In this work, however, we consider only homogeneous densities.

Another popular approach is the mass-concentration (mascon) approach. Here, a body of arbitrary shape is subdivided into small mass elements, so-called mascons. Decreasing the mascon size increases the accuracy, however, this also leads to an increasing computation time. Other than for the PM, there are different implementations of this method. The both mascon methods *Mascons - Sphere Packing (MSP)* and *Mascons: Spherical coordinates (MASC)* are also used in this work and introduced in Section 3 with the PM. Two other mascon implementations were presented by [5], using uniform-sized cubes and spheres. Note that the potential of the individual cubes was calculated using the expression used for the PM [6]. A combination of the mascon and spherical harmonics approach was proposed by [9]. The basic idea is to discretize a model of Phobos into small cubes, and then evaluate the spherical harmonic gravitational field of each individual cube.

Method Comparisons

While there is a multitude of works using the different gravitation field computation methods introduced in the previous paragraph, the inter-comparison between different methods as done in this work is still limited.

The single-sized sphere and cube mascon approaches were compared by [5] with the PM method on the example Itokawa. Relatively large deviations were found close to the surface that diminished with increasing altitude. Note that [5] also compared the difference in gravitational field between a single cube and sphere, however, this is not to be confused with the comparisons made in Section 5.

Another comparison was done of the MSP with the PM by [10]. The bodies compared were the asteroids Itokawa and Lutetia, as well as Eros, however, the presented results were limited to altitudes of 100 m and 1 m *above* the surface, and therefore did not include comparisons directly *on* the surface.

In [11] the authors have proposed a finite element method to compute the gravitational potential and gravitation with tetrahedra. Their method combines the mascon and polyhedral methods. After the conventional division technique (tetrahedralization) they have used the polygon method for each tetrahedron and also compared it to the polygon method for the whole asteroid 216 Kleopatra as an example. Their errors seemed to be very small and limited by floating-point precision, but they have not provided any run-time information.

A comparison between the finite cube elements method and shapes with an analytical solution for gravitation was done in [12]. The cubes were approximated as spheres because it allows an easy calculation of gravitation and also reduces the running time. Moreover, they have investigated a fractal object, the effects of choosing a structural index SI, which is a measure of the degree of homogeneity of gravity/magnetic equations and they focussed on solving the inverse problem: estimating the inner structure of asteroids with Euler deconvolution.

3. METHODS

This work uses and compares a total of three methods:

- the *Polyhedral Method (PM)*,
- the *Mascons - Sphere Packing (MSP)* method, and
- the *Mascons - Spherical coordinates (MASC)* method.

When referring to *mascon methods*, we refer to both methods MSP and MASC. In the following, each of these methods is introduced in detail.

Polyhedral Method (PM)

The polyhedral method (PM) is a well-known analytical closed-form approach to compute the exterior gravitation of any polyhedron shape developed by [6]. One big advantage is that this method is valid and stable down to the body's surface, i.e. also inside the circumscribing Brillouin sphere, where e.g. spherical harmonics are prone to divergence. This makes the methods interesting for surface gravimeter science [13], [14] and landing operations [15], [16], as well as touch-and-go maneuvers [17]. On the downside, however, the method only works for a homogeneous (constant) density throughout the body and does not intrinsically allow to vary the density within the shape. While this method works even on the surface of the body, it is undefined on a vertex or edge which limits the solution space of the cube analysis (Section 5).

For the PM, we use an algorithm implementation developed by [18] with minor adaptations. This code was verified with an independent PM implementation, provided by [19]. The gravitational attraction can be expressed as

$$g(x) = -G\rho \sum_{e \in edges} E_{ij} \cdot \vec{r_{ij}} \cdot L_{ij} + G\rho \sum_{e \in facets} F_{ijk} \cdot \vec{r_{ijk}} \cdot \omega_{ijk} \tag{1}$$

where we refer to [6] for the full derivation and to [19] for a slightly adapted notation.

Mascons: Sphere Packing (MSP)

Our second competing method is based on mascons. In general, the idea behind the mascon model is to subdivide a body into smaller parts, called *mascons*. The gravitational field of each of these mascons is calculated by concentrating the mass of this element in its center and computing the gravitational field of a point source. Integration over the mass elements then yields the resulting gravity. Traditionally, mascons are often represented as uniform cubes or spheres. The MSP method uses a slightly different approach: the main idea is to use a *polydisperse sphere packing*, i.e. the spheres are all inside the shape, they are allowed to differ in their radii and they do not overlap each other. This should lead to a better distribution of the mascons for faster computations times and higher accuracy.

Moreover, spheres allow an easy computation of gravitational acceleration at any point. If we consider a set of n spheres, then we can compute the gravitational acceleration at a given point $\mathbf{x}$ as follow:

$$\mathbf{g}(\mathbf{x}) = \sum_{i=1}^{n} \frac{GM_i}{||\mathbf{r_i}||^2} \hat{\mathbf{r}}_\mathbf{i} \tag{2}$$

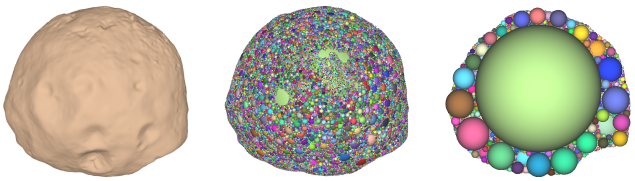

(a) (b) (c)

Figure 1: In 1a is a polygonal mesh of Phobos (275k triangles, [21]) with the corresponding sphere packing in 1b (800k spheres, generated with Protosphere [20]) and a cross-section of the packing in 1c.

with $\mathbf{r_i} = \mathbf{c_i} - \mathbf{x}$ the vector between the sphere center c_i and given point x. M_i is the mass of the sphere and G the gravitational constant. We also easily parallelize the computation of Equation 2: For each mascon, a thread is running to compute

Algorithm 1 Gravity(SpherePacking S, QueryPoint x)

for all *spheres* $s_i \in S$ **do in parallel**
$r_i = c_i - x$
$\mathbf{g_i}(\mathbf{x}) = \frac{GM_i}{||\mathbf{r_i}||^2}\hat{\mathbf{r}}_\mathbf{i}$
end for
parallel scan over all g_i compute $g(x) = \sum_{i=1}^{n} g_i(x)$

the gravitational acceleration and a parallel scan sums up the accelerations. We have two main challenges with the mascon model: the arrangement of mascons and the assignment of masses to the mascons.

Sphere Packing Arrangement—We use spheres to represent the mascons, therefore we have to subdivide the space with spheres. Unfortunately, we can not achieve a complete covering of the targets volume. From Kepler conjecture, we know that uniform spheres can cover at most $\frac{\pi}{\sqrt{18}} \approx 74\%$ of the target volume. We use polydisperse sphere packings, to cover potentially more volume than that.

An Apollonian sphere packing is a fractal structure based on rules. That idea was extended in [20] to arbitrary 3D objects, which we use here. It uses a greedy algorithm that prefers larger spheres. The result is a potentially space-filling sphere packing (see Figure 1). The spheres do not overlap and they are completely inside the 3D object.

Compared to methods presented in [22], that place spheres in a fixed grid, Protosphere is more robust, faster, and has a better filling fraction. The greedy choice of the largest spheres provides a level-of-detail automatically. A very simple solution would be to limit the number of spheres if spheres are in descending order with respect to their size.

With no modifications, Protosphere generates sphere packing fractions of more than 90% for most asteroid-like objects with 100k spheres. This packing density is more than 5% higher in [22]. Our higher packing density should improve the gravitational field estimation. It is possible to define the minimum and maximum size of spheres for packing and we can change the optimization criteria for packings to influence the arrangement. We have tried to place more spheres near the surface, which lead to an unexpected increased error for the gravity at the surface. Therefore, we present here our results using the standard greedy implementation and keep investigating the previous issue.

Mass Assignment for Spheres—In the second step, we assign masses to the spheres, which are inside the 3D mesh. The total mass M of an asteroid must be equal to the sum of all mascons. It is not trivial to assign masses to the mascons, especially when using sphere packings. The voids between the spheres can lead to significant errors. The difference in sphere sizes leads to an inhomogenous void distribution. To solve this problem, we use our method that we call "Delta percentage volume increase" (DPVI). Typically, smaller spheres have a higher proportion of empty volume in their neighborhood, so the idea is to increase smaller spheres more than larger spheres. We set the volume of a sphere to $V_i + \frac{V_i \cdot x}{r_i}$, where V_i is the volume, r_i the radius of the sphere, and x is obtained through Equation 3, which includes the constraint that the sphere packing volume after incrementing has to be equal to the volume of the polygonal model V_p.

$$x = \frac{V_p - \sum_{i=1}^{n} v_i}{\sum_{i=1}^{n} \frac{v_i}{r_i}} \tag{3}$$

To compute the individual radius increase δr_i of each sphere, the following cubic equation can be solved:

$$\frac{V_i \cdot x}{r_i} = \frac{4\pi(r_i + \delta r_i)^3}{3} \tag{4}$$

With the final volume or radius of a sphere, a corresponding mass can be assigned considering a homogenous density.

Mascons: Spherical coordinates (MASC)

The second mascon method models the internal mass distribution of the body as a set of solid elements in spherical coordinates. The software package hereafter referred as *MASC* was originally developed to derive gravity field coefficients based on shape and internal density distribution and has been successfully applied to the Mars moon Phobos [23] and the 67P/Churyumov-Gerasimenko [24]. It was for this study extended to compute in addition the gravitational acceleration acting on a spacecraft at a certain position. The structure of the software is divided into three parts:

1. In the first part, the provided shape model is divided into longitudes ϕ and latitudes λ with an a priori specified resolution to ensure the accuracy of the derived quantities. Different shape models such as analytical shapes (sphere, ellipsoid), a spherical harmonics representation of shape, and SPICE shape models can be processed [25].
2. The next step is to structure the already processed shape model into sub-volume elements by dividing also the radius R with a specified length (see Figure 2). Each of these volume elements is assigned a specific density ρ that defines the mass of that element. Spherical harmonics and moments of inertia are outputted and a table of mass elements with their according center of mass position $\vec{c}_i$ as an entree for the next processing step.
3. In the last step, the total acceleration acting on a spacecraft at position $\vec{x}$ is computed as the sum of the accelerations of each of the beforehand defined mass elements $m_i = v_i\rho_i$ according to Equation 2.

4. Test Cases

Before presenting the results in the following three sections, we introduce the three test cases and the general test setup that ensures comparable results. The three test cases are

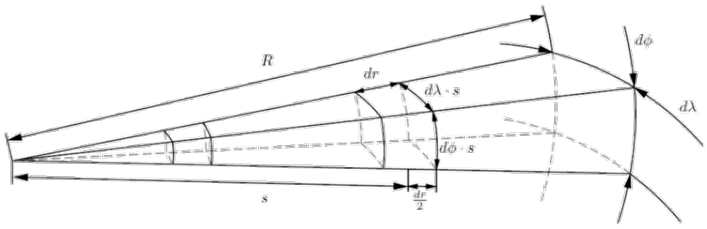

Figure 2: Subdivision of the shape model into small mass elements with MASC.

1. Homogeneous sphere for the comparison with an analytical solution
2. Homogeneous cube for the comparison with an analytical solution
3. Homogeneous Phobos test case

More details on the individual methods are provided in their corresponding subsection. All methods use the same value for the gravity constant: $G = 6.674 \cdot 10^{-11} \frac{Nm^2}{kg^2}$ and the analytical cases use the homogeneous (arbitrary) density $\rho = 1000 kg/m^3$, while the third case uses the density of Phobos used by [21], $\rho = 1860 kg/m^3$.

Obviously, for a sound comparison, the gravitation evaluation points need to be identical for all methods. As the PM is not defined at the polyhedron vertices (Section 3) we decided to take the center-point of each facet as the evaluation point as the center of the three vertices i, j, k.

$$\begin{bmatrix} x_{eva.} \\ y_{eva.} \\ z_{eva.} \end{bmatrix} = \frac{1}{3} \begin{bmatrix} x_i + x_j + x_k \\ y_i + y_j + y_k \\ z_i + z_j + z_k \end{bmatrix} \tag{5}$$

Initially, we also created evaluation points "on-orbit" on five concentric spheres, however, the deviations between the results were, as expected, largest on the surfaces of the three shapes/bodies. Consequently, we will limit the analysis of the results to the above-described surface points. Without question, the evaluation points of the analytical solutions are identical to the ones used for the three methods.

Test Case Sphere

For the sphere test case, we chose a perfect sphere with a radius of 1km. The sphere case is interesting and challenging because the representation of such an ideal sphere is not possible with each method. Besides this difficulty, it has a simple analytical solution, which makes it attractive for comparisons.

Considering a perfect sphere, the following statements can be postulated regarding the resolution (res) and the difference between computation and true solution (diff):

- The MSP method could fill the sphere with a single sphere, leading to a perfect match between method and analytical solution, thus diff $= 0$.
- The MASC method will converge to the true solution using a high resolution, i.e. for res$\rightarrow \infty$ the diff$\rightarrow 0$.
- The PM cannot analyze a perfect sphere, as implied by the name, we need a polyhedron that approximates the sphere, similarly, as the number of polyhedron facets n $\rightarrow \infty$ the diff$\rightarrow 0$.

To solve the representation problem, we have decided to use two different kinds of parametrizations of the sphere. Our first sphere is based on an icosahedron, that has 20 triangles. After two successive subdivisions we obtain an icosphere with 320 triangles (see Figure 3a). On each edge of a triangle, a new triangle point is created and scaled to the sphere radius. Therefore, the number of triangles grows with $20 \cdot 4^n$. The second sphere is based on spherical coordinates, which means we can subdivide the sphere with two angles respectively longitude and latitude (UV sphere, see Figure 3b). This method allows more freedom to aim for a specific number of triangles. At first, we created six icospheres with an increasing number of triangles, because of the limited freedom of the algorithm. Then we used the number of triangles from the icospheres as a reference, that we manually approximated for the six UV spheres while we were keeping the ratio between longitude and latitude constant.

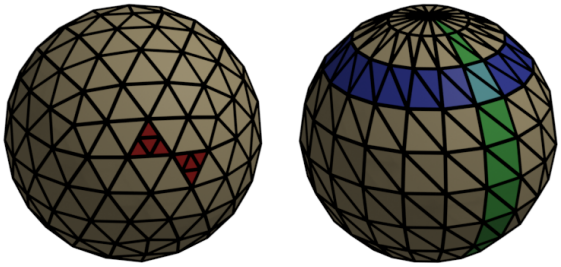

(a) Icosphere with 320 triangles. Triangle-subdivision (red): One triangle is divided into four triangles.

(b) UV-sphere with 360 triangles. Subdivision in longitude (green) and latitude (blue).

Figure 3: Spherical shapes with the lowest resolution we have used. Colors indicate the two subdivision processes.

In the sphere test case, our evaluation points are not the triangle center of the different spherical shapes. Instead, our evaluation points are lying on a perfect sphere with each point having a norm that is equal to our chosen radius (1km). We chose the points based on an icosphere with 81920 triangles. Then we computed the center points of the triangles and scaled them equal to the radius of our ideal sphere. Of course, all our spherical shape models approximate that ideal sphere and constant chosen radius. For each individual method, we assess the deviation from the true solution as a function of the shape triangulation and number of facets.

Test Case Cube

Our second test case is a cube with an edge length of 2km. Unlike a sphere, a cube can be easily defined through a polygonal model. We use a polyhedron of $6 \times 2 = 12$

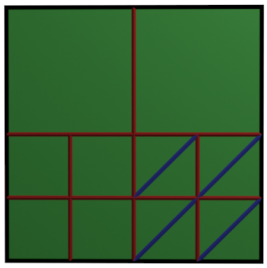

Figure 4: Subdivision iterations (red) of a cube face (green) in equal-sized quads and after triangulation (blue) the evaluation points are the centroids of the triangles.

triangular facets. However, the sharp-edged shape of a cube is more challenging for methods based on spherical mascots. Like the sphere, the cube allows an analytical solution to compute the gravitational field by using existing analytical expressions for right rectangular prisms.

Different analytical expressions for a right rectangular prism were reviewed in [26]. We use the analytical expression derived from Okabe [27] for the vertical component of gravitational acceleration as given in Equation 6:

$$g_z = -G\rho \sum_{i=1}^{2}\sum_{j=1}^{2}\sum_{k=1}^{2}(-1)^i(-1)^j(-1)^k \Bigg[x_i \ln(y_j + r_{ijk}) + y_j \ln(x_i + r_{ijk}) + 2z_k \arctan \frac{x_i + y_j + r_{ijk}}{z_k} \Bigg] \quad (6)$$

with

$$x_i = x - \xi_i, \quad y_j = y - \eta_j, \quad z_k = z - \zeta_k \quad (7)$$

$$r_{ijk} = \sqrt{x_i^2 + y_j^2 + z_k^2} \quad (8)$$

The sides the cube are parallel to x, y, z axes and its dimension is defined by $\xi_1 \leq \xi \leq \xi_2, \eta_1 \leq \eta \leq \eta_2, \zeta_1 \leq \zeta \leq \zeta_2$. Other gravitational components g_x and g_y, can be obtained through cyclic permutation.

To determine the evaluation points on the cube surface, we did first a subdivision of each face like in Figure 4. Then we triangulated the quad and used the triangle centers as evaluation points. With n iterations, the number of triangles grows exponentially: $2 \cdot \#facets \cdot 4^n$. We use six iterations respectively 49.5k evaluation points on the cube surface, since this resolution already highlights differences very well. Similarly, the evaluation points could have been chosen based on a grid with a specific resolution.

Phobos

For our last test case, we have chosen the Martian inner moon Phobos. Phobos is an applicable case because the still ongoing Mars Express mission is able to perform close flybys at Phobos [28]. Another Phobos mission is already on the horizon, the Japanese MMX spacecraft [16], which will visit the Mars moon and observe it from a Quasi Satellite Orbit (QSO) in the mid-2020s. The carried simulations in this paper can support the planning of future observations and the analysis of data from the two missions. We use the high-resolution shape model provided by [21]. Also, Phobos has one remarkable large crater *Stickney* and a large number

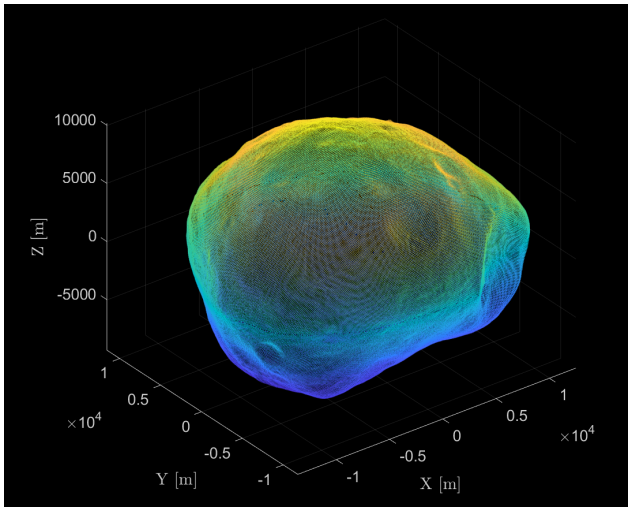

Figure 5: Vertices of Phobos Wavefront (OBJ) file from [21] used for the gravitation comparison.

of smaller craters which are very well resolved in the shape model (see Figure 5). Additionally, this offers a realistic shape that is more complex than the sphere and the cube. Regarding the gravity evaluation points on the surface, we compute them as the centers of each triangular facet.

5. Results

In this section, we provide the results of our systematic evaluation of the different methods in the three scenarios. First, we show detailed graphical and numerical comparisons for the sphere (Section 5) and cube (Section 5) test cases with their respective analytical solution for different parameter settings like parametrization or polygon count. Finally, we compare results of the different methods for the Martian moon Phobos test case. In this scenario, we set the PM method as the ground truth, considering a homogeneous density throughout the body, and show the differences to the two different mascon methods.

The *relative* comparison is done taking the ratio τ of the resulting gravitational acceleration of the numerical computation g_{num} to the analytical solution g_{ana} as:

$$\tau = \frac{g_{num}}{g_{ana}} \cdot 100\% \quad (9)$$

Therefore, a ratio $\tau < 100\%$ represents an under-estimate of the gravitational acceleration, $\tau = 100\%$ is a perfect match, and $\tau > 100\%$ represents an over-estimate (over-shoot) of the gravitational acceleration.

Our results were computed on different hardware, with double-precision floating-point numbers on each platform:

- PM (CPU): Intel® Core™ i7-8850H (Matlab)
- MSP (GPU): NVIDIA GeForce RTX™ 3080 (CUDA)
- MASC (CPU): Intel® Xeon® Gold 6134 CPU using 32 threads (Fortran).

It should be noted that different hardware is used for the three models, which is why the specified calculation times cannot be directly compared. However, the general tendency of the computation times is obvious.

Comparison with Analytical Sphere Model

The gravity field of the perfect sphere with radius r has a simple analytical solution as we can see in Equation 2. Therefore, in the first step, we compare this analytical solution to the results of the three investigated methods.

For the PM method, the computation time increases with an increased number of faces, which we also report. While the computation times were recorded on different machines for the three methods, the relative change compared to the improvement in accuracy provides insights to the relation between time vs. accuracy in gravity computation for the different methods.

The polyhedral method was applied to the icospheres and UV spheres for the different number of facets. The comparison with the analytical solution is shown in Figure 6 for the icospheres and in Figure 7 for the UV spheres. The colorbar is always interpolated between the min. and max. values, so the interpretation is done with the values listed in Table 1. Note that the comparison is done directly on the surface where the differences are maximal. Generally, with the polyhedron not exceeding the perfect sphere, the total mass of the polyhedral volume will be always smaller than the analytical solution given the same density, which results in a smaller gravitational acceleration. This difference becomes smaller with higher resolution. But also a variation in the deviation patterns exist for the different shape models, especially, when comparing the coarsest resolutions of only 320 (icosphere) and 360 (UV sphere) facets, respectively.

For the icosphere, there are hexagonal regions of overshoot and underestimation of the gravitation, clearly visible for the lowest resolution (Figure 6a). When increasing the resolution, two observations can be made, repeating that the range of differences decreases: Firstly the individual regions of over- and undershoot decrease in size while the number of these regions increases. Secondly, these regions begin to group in larger regions (Figure 6b, 6b, 6c, 6d), eventually forming very large regions of over- and undershoot, decreasing the number of these regions to 4 regions of overshoot and eights regions of underestimation for the plotted visible hemispheres (Figure 6f).

In contrast, the results for the UV sphere forms a quite different pattern. The (dark blue) regions of the underestimation form circular regions, while lesser underestimates form diamond-like shapes (Figure 7a, 7b, 7c). At the "equator", these overshoots are individual regions, while they grow together forming latitudinal bands towards the "poles". Other than for the icosphere, for the UV sphere, these features become continuously smaller, not forming visible global patterns (Figure 7d, 7e, 7f).

The reason for this different behavior, depending on the parametrization of the sphere, is based on the icosahedral symmetry: our icosphere is based on the icosahedron. Consequently, all vertices have exactly six adjacent triangles, except 12 vertices which have five adjacent triangles. This results in the soccer ball-like pattern that we observe for the icosphere. Triangles become smaller, the closer they are to these 12 icosahedron vertices. This means, the triangles are not distributed equally but in the proximity of the icosahedon vertices we have a higher frequency.

In contrast, for the UV sphere, the vertices are defined through spherical coordinates. If we increase the resolution, then we have also more vertices touching the ideal sphere surface along the latitude and longitude circles and the sizes of the triangles depend on the spherical distance to the equator. This is a regular pattern that we can observe in our Figure 7.

Finally, the relative (mean) error is compared with the computation time in Figure 8. It can be observed a clear saturation, where initial increases in the number of facets have a significant influence on the achieved accuracy of the gravitation, whereas the last step for both spheres adds only little accuracy while increasing the computation time each by more than a factor 4.

Overall, it can be concluded that while computationally expensive, and detailed (large) shape files are needed, it is well possible with the PM to approximate an ideal sphere. However, this method intrinsically does not allow the perfect gravitation assessment of spherical/round shapes, or surface features, and therefore remains an approximation for such features, limited by the shaped file (observation) resolution.

The MSP approach works internally with ideal representations of the spheres, therefore it includes the analytical solution and a possible comparison would result in zero (beside floating-point limitation).

Hence, we additionally decided to fill the polygonal shapes with a single sphere. With our one-single sphere packing, we covered a relatively high amount of volume. However, this covered volume is not important in this case: For a single sphere, the mass assignment is trivial, it is the density multiplied with the volume of the whole spherical shape. It can be seen as a single point mass and because of that, our results reported in Table 2 should state the most accurate results we can theoretically get from each spherical shape model. It can also be seen as a conversion from a polygonal sphere model back to an ideal sphere model. This enables us to measure the mean error for the conversion to a polygonal model: If our ideal sphere has the mean surface gravity G_i and our shape model has G_s as the mean surface gravity, then the mean approximation error is $G_i - G_s$. By using one sphere we can see a small and constant computation time (1.4s) compared to PM and MASC.

When we compare the PM to MSP, we can see that the gravitational acceleration results are getting closer with higher shape resolution in general. However, the results for the UV sphere are closer together than for the icospheres. We assume that the reason for it might be the way we have chosen our evaluation points for the sphere test case.

The MASC approach uses spherical coordinates to subdivide the shape into mascons. Therefore, shapes similar to spheres are favorable for a high accuracy computation of the acceleration. Due to the limitation by the shape, i.e. the perfect spherical shape is only approximated by icospheres or UV spheres, the PM method provides a good solution besides the analytical expression or trivial mascon method (one point mass).

MASC provides the ability to model and subdivide a perfect sphere into mascons. The resulting surface acceleration can be approximated using 64.8k mascons with an overall mean difference to the analytical solution of 0.0007% for example. As it can be seen in Table 3, the accuracy obtained with MASC is close to the results from PM and MSP. For all different shapes, 64.8k mascons have been used and therefore, the computation time is also identical for all cases.

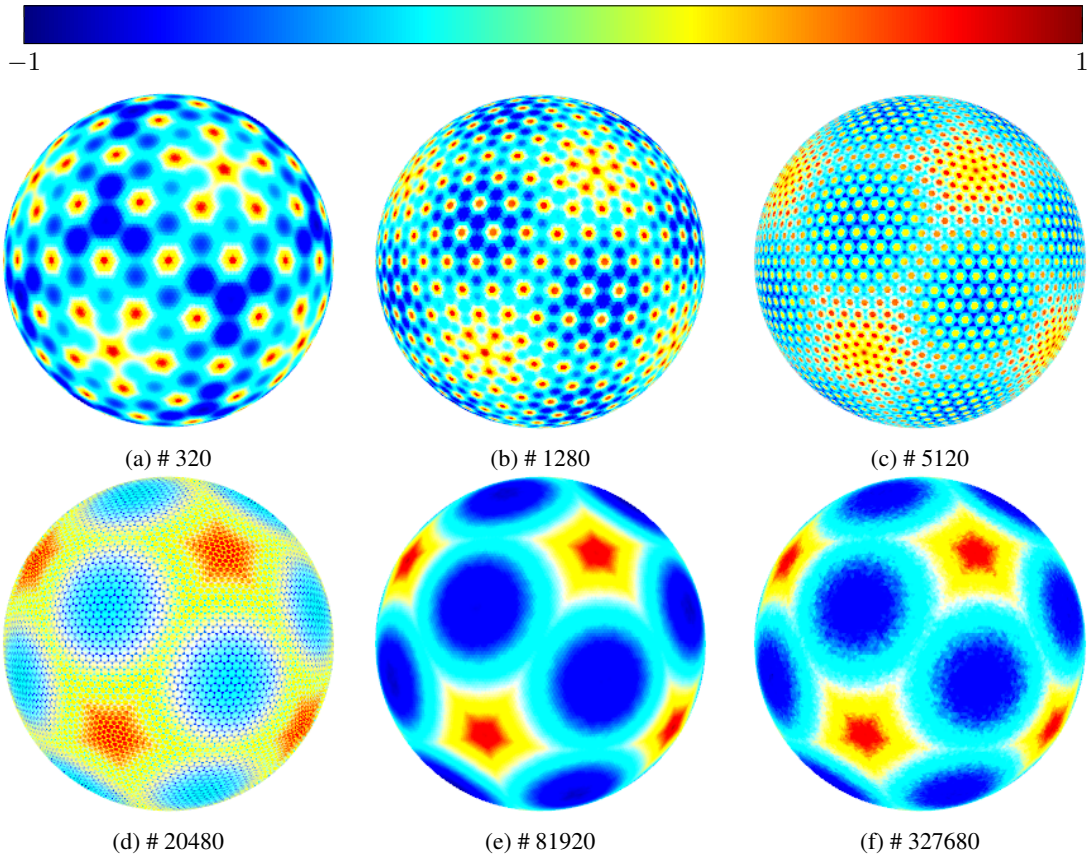

(a) # 320 (b) # 1280 (c) # 5120

(d) # 20480 (e) # 81920 (f) # 327680

Figure 6: Icospheres with the number of faces. Using PM for individual surface gravity visualization: min. (blue) and max. (red). Visualization is identical with the min. and max. values from Table 1.

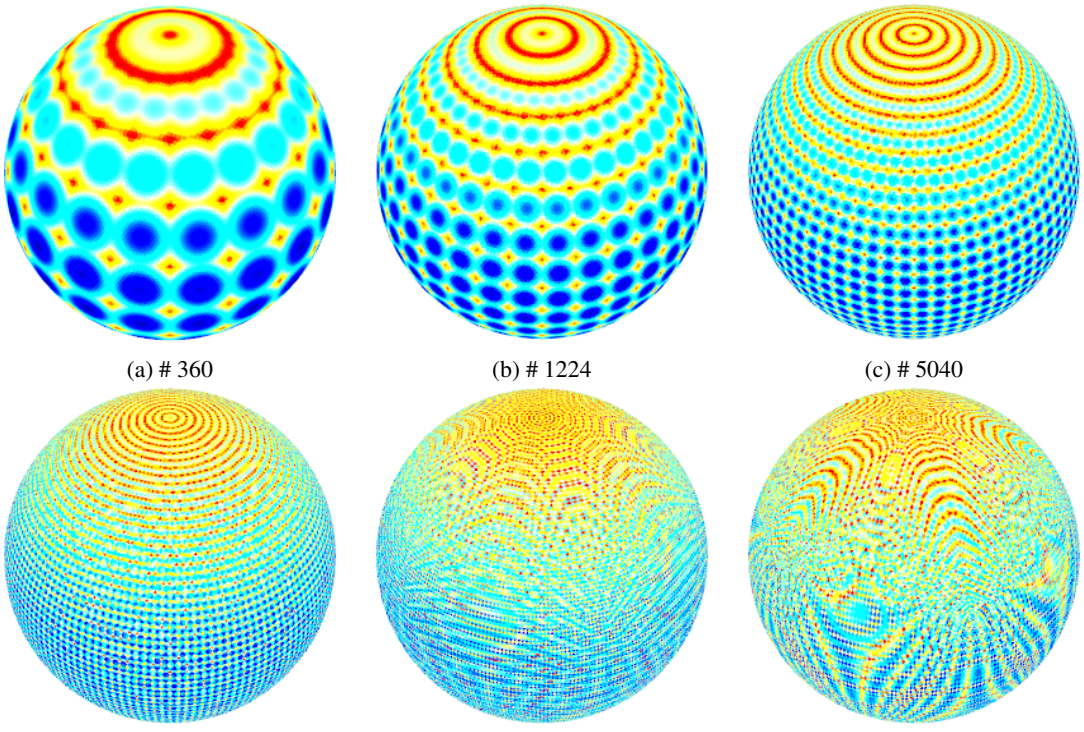

(a) # 360 (b) # 1224 (c) # 5040

(d) # 20448 (e) # 82368 (f) # 328328

Figure 7: UV spheres with the number of faces. Using PM for individual surface gravity visualization: min. (blue) and max. (red). Visualization is identical with the min. and max. values from Table 1.

Table 1: Comparison of gravitation computed for different sphere shape models using the PM, compared to the analytical solution. Due to the approximated polyhedron lying within the perfect sphere, all values are below 100 %. All values in percent, giving the ratio of the PM to the analytical solution. Additionally, we provide the corresponding computation times T_{comp} and the standard deviation over the full surface σ.

Shape	**Min. [%]**	**Mean [%]**	**Max. [%]**	σ **[%]**	$T_{comp.}$ **[s]**
ico:320	95.8599	96.6437	97.9965	0.3968	27.3
ico:1280	98.9134	99.1447	99.4826	0.1121	73.2
ico:5120	99.7232	99.7836	99.8566	2.7918E-2	277.1
ico:20480	99.9302	99.9442	99.9578	5.4776E-3	345.3
ico:81920	99.9825	99.9844	99.9878	1.2096E-3	2,710.5
ico:327680	99.9955	99.9960	99.9970	3.0489E-4	12,749.2
uv:360	94.6775	95.9555	97.8482	0.6550	28.2
uv:1224	98.2785	98.7374	99.3877	0.2242	68.1
uv:5040	99.5589	99.6832	99.8505	5.9350E-02	266.0
uv:20448	99.8887	99.9209	99.9632	1.5308E-02	642.7
uv:82368	99.9702	99.9793	99.9905	4.0139E-03	2,597.6
uv:328328	99.9931	99.9954	99.9979	9.4118E-04	11,233.3

Table 2: Comparison of gravitation computed for different sphere shape models using the MSP with a single sphere, compared to the analytical solution in percent. G_s can be interpreted as a theoretical limit for each spherical shape. MMM. stands for Min., Max., Mean and is equivalent to mean gravity G_s. The last columns compare other methods to G_s.

Shape	**MMM.,**G_s **[%]**	σ **[%]**	$T_{comp.}$ **[s]**	**PM** $-G_s$ **[%]**	**MASC** $-G_s$ **[%]**
ico:320	96.6152	9.2827E-11	1.4	0.0285	0.0127
ico:1280	99.1380	6.8273E-11	1.4	0.0067	0.0039
ico:5120	99.7835	1.0206E-10	1.4	0.0001	0.0011
ico:20480	99.9458	1.2944E-10	1.4	-0.0016	0.0004
ico:81920	99.9864	1.7308E-10	1.4	-0.0020	0.0003
ico:327680	99.9966	4.8705E-11	1.4	-0.0006	0.000
uv:360	95.9561	1.3250E-10	1.4	-0.0006	0.0083
uv:1224	98.7372	9.6639E-11	1.4	0.0002	0.0002
uv:5040	99.6832	1.2205E-10	1.4	0.0000	0.0001
uv:20448	99.9208	1.2052E-10	1.4	0.0001	0.0003
uv:82368	99.9793	1.3138E-10	1.4	0.0000	0.0001
uv:328328	99.9955	8.3166E-11	1.4	-0.0001	0.0000

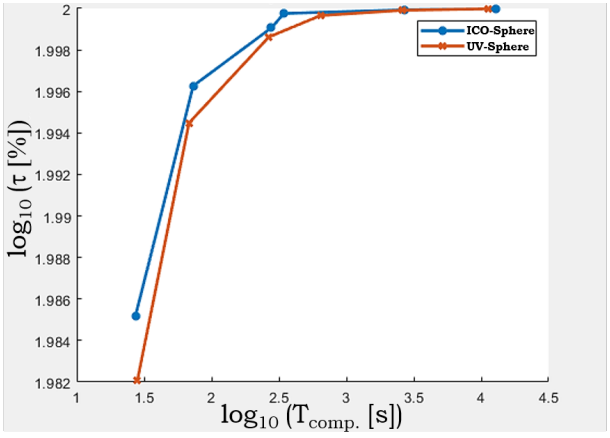

Figure 8: Comparison of mean error of τ as a function of computation time (and therefore number of facets as listed in Table 1).

The small difference between the results MASC and PM or MSP can be explained on the one hand by the selected resolution, but the effect should be small as shown above for the perfect sphere case. The other contribution to the difference is the fact that MASC computes the center of the mascons not at the center of the facets as it is the case for PM. This leads to mascons used by MASC which do not perfectly match the facets of the shape. It can be concluded that MASC provides a similar accuracy as PM for different shape representations for a sphere.

All three methods are capable to compute the gravitational acceleration of a sphere on the surface with a high resolution. Modeling a perfect sphere is very favorable for MSP since it can be realized with just one single sphere. The needed computational time for MASC and MSP are independent of the resolution of the shape model whereas for PM is dependent on the number of facets of the used shape model. It should be noted that the icosphere shape always provides a better approximation than the UV sphere when compared to the analytical solution.

Table 3: Comparison of the gravitational acceleration computed for different sphere shape models using the software package MASC, compared to the analytical solution. All values in percent, giving the ratio of the MASC results to the analytical solution. The corresponding computation times $T_{comp.}$ are identical for all cases since the same resolution is used (64.8k mass elements).

Shape	**Min. [%]**	**Mean [%]**	**Max. [%]**	σ **[%]**	$T_{comp.}$ **[s]**
ico:320	96.4633	96.6279	96.8495	0.1000	47
ico:1280	99.0958	99.1419	99.2062	0.0289	47
ico:5120	99.7718	99.7846	99.8017	0.0075	47
ico:20480	99.9421	99.9462	99.9541	0.0022	47
ico:81920	99.9847	99.9867	99.9954	0.0013	47
ico:327680	99.9957	99.9966	100.0056	0.0013	47
uv:360	95.5245	95.9644	96.7512	0.3782	47
uv:1224	98.5980	98.7374	99.0073	0.1242	47
uv:5040	99.6471	99.6833	99.7531	0.0313	47
uv:20448	99.9120	99.9211	99.9382	0.0075	47
uv:82368	99.9760	99.9794	99.9861	0.0021	47
uv:328328	99.9942	99.9955	100.0041	0.0012	47

Table 4: Comparison of cube gravitation computed for the three different methods compared with the analytical solution. For the PM, the order of magnitude of the deviation is given.

Method	**Min. [%]**	**Mean [%]**	**Max. [%]**	σ **[%]**
PM	$100 - 10^{-12}$	100	$100 + 10^{-12}$	10^{-13}
MSP 100k	98.6829	100.0534	100.9607	0.2992
MSP 300k	99.1722	100.0394	100.6124	0.1948
MSP 600k	99.2450	100.0300	100.4872	0.1531
MASC 64.8k	84.7789	101.8223	109.4622	5.6377

Comparison with Cube

The analytical solution for gravitational acceleration on the surface of a cube is provided in Figure 9a and the comparison of the three methods with the analytical solution is summarized in Table 4.

With the representation as a polyhedron, PM provides an analytical solution, and hence we only provide the order of magnitude of the deviation, caused by the numerical computation. However, as stated in Section 3, the PM is not defined on the edges/vertices of the shape, where the method returned NaN. For the comparison here, we have excluded these evaluation points, but have noted the limitation of this method here.

The comparisons of the three methods to the analytical solution are plotted in Figure 9b and 10. In black, the excluded values for the PM are visible due to the absence of the numerical solution here.

The analytical solution and the quasi-identical PM solution clearly show symmetry of the gravity field, and therefore perface. The same is true for the MASC solution, but not for the MSP.

With the MSP we have created three different packings. We have linearly increased the number of spheres in the packings, ranging from 100k to 600k. From Table 4, we can see an improvement in every category with increasing the number of spheres, as we would expect from a mascon method. Also, we can see that the improvement seems not to be linear with an increasing number of spheres. The most important observation is probably the tendency of overshooting. In Figure 10a we can clearly see a reddish noise pattern. The reason is our mass assignment heuristic: if we would naively just assign the mass to the homogeneous spheres and not consider the empty volume, we would have an overall underestimate. Instead, our heuristic assigns proportionally more mass to smaller spheres which is the reason for the reddish overshooting pattern. If we increase the number of spheres, this produces also smaller spheres close to the surface. Hence, it could be expected that the error at the surface would increase, but the opposite is the case. Our average error decreases with more spheres. An undershooting can be observed at the edges and a circular pattern at the cube face centers. The reason for these edges is that the relative large spheres are placed elsewhere and our greedy algorithm prefers them. This problem is demonstrated in Figure 11. From that figure, we can also observe, that we have a large sphere in the cube center, which leads to the circular pattern at the center of the cube faces. The spheres are getting smaller when we are going to the face center and at some distance from the face center, there are no small spheres (blue circles, Figure 10a), since we have a fixed number of spheres. So we observe a gradient from under- to overshooting going to the face center.

Subdividing a rectangular shape like a cube in spherical coordinates shows the disadvantage of the method used within MASC. It can be clearly seen in Figure 10b that there is an underestimation of the acceleration at the edges of the cube, where the shape cannot be approximated precisely. At the center of each surface, the acceleration is in very good agreement with the analytical solution. But moving towards the outer edges of the cube the gravitational acceleration is overestimated by a small portion. The difference to the analytical solutions becomes in the following smaller until the underestimated regions at the corner and edges are reached. It is obvious that the mascons in spherical coordinates are not a good choice to approximate rectangular shapes. A higher resolution would help to overcome the problem but with the cost of a much higher computational effort.

As the results were produced on different machines, we do not compare the computations times here. Qualitatively, we

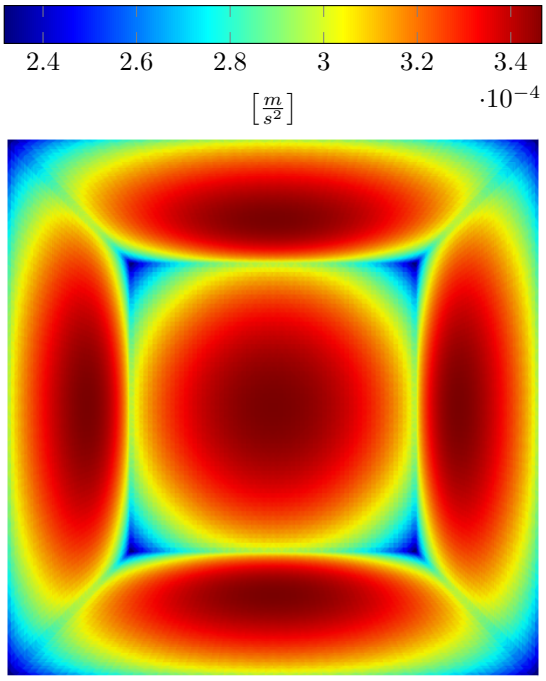

(a) Cube with analytic solution [27]. The surface gravity of five faces: min. (blue) and max. (red). The center of each cube's face is showing the highest gravitational acceleration.

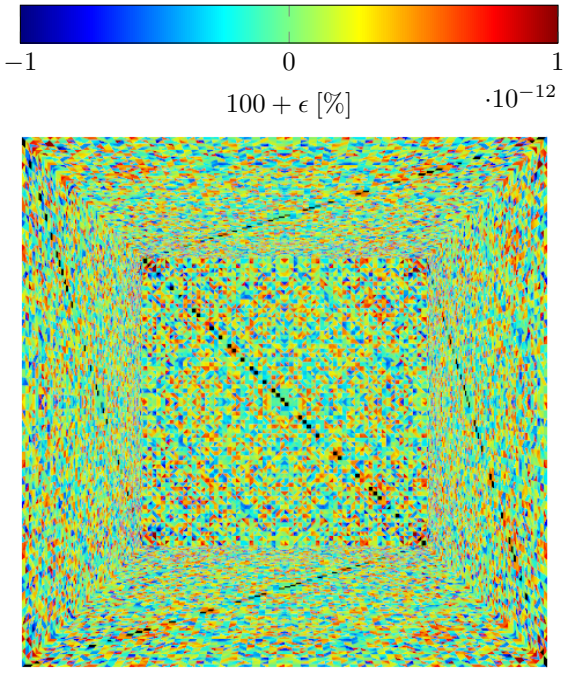

(b) As expected, the agreement between PM and analytical solution is quasi-perfect. The five edges cutting the 5 faces are partly visible (black) where the PM is not defined on the edges.

Figure 9: Surface gravity of the cube and percentage difference between analytic solution (reference) and PM.

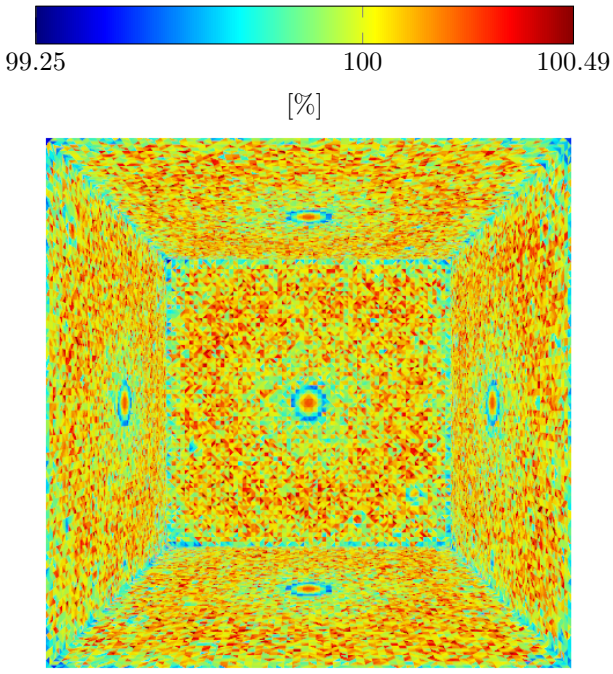

(a) MSP 600k. Smaller undershooting at the 12 edges and larger at the face center. Also, overshooting between edges and face center.

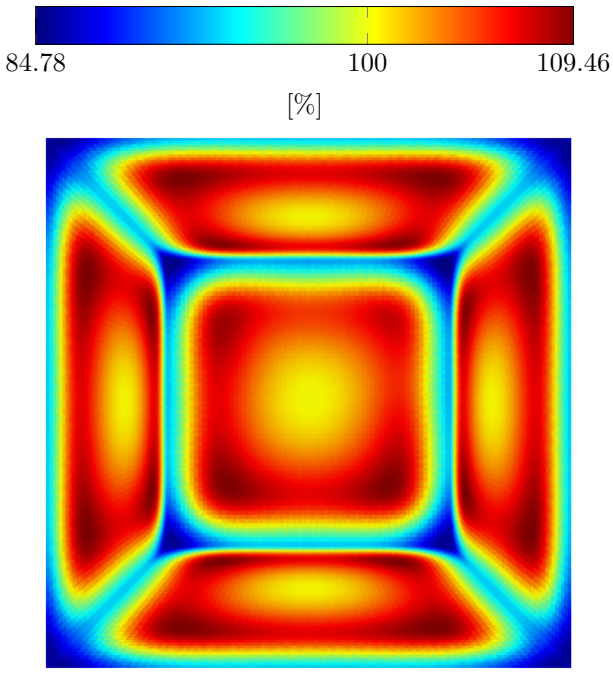

(b) MASC. Clear undershooting at the 12 edges. Also, a square-like overshooting between edges and face center.

Figure 10: Using percentage difference to PM as reference for surface gravity: overshoot (red) and undershoot (blue).

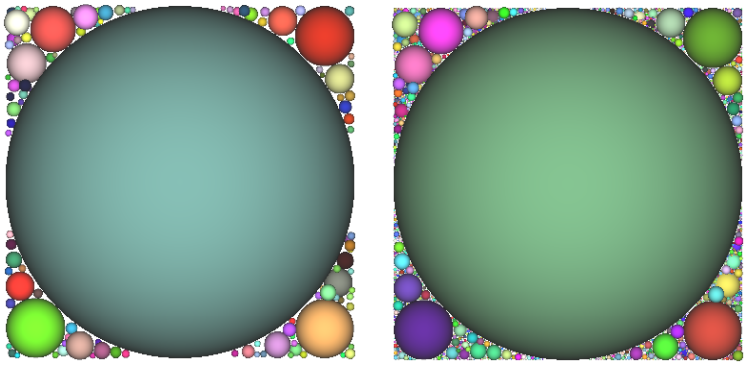

(a) 10k Spheres (b) 600k Spheres

Figure 11: The cube is a challenging case for the MSP method: the left-hand side shows an example of problems with non-uniform distribution and packing density. Compare the top left corner of the cube with the other corners, and see the gaps at the centers of the cube's sides. More spheres improve these issues, see the right-hand side. (Both images show the same cross-section.)

can state that here the PM benefited most from the rectangular shape, reducing the computation time to tens of seconds for a comparable number of evaluation points, as the number of facets (12) was very small, driving the computation time complementary to the number of evaluation (field) points. MASC is using the same number of mascons (64.8k) as for the sphere case. Therefore, the computation time depends only on the number of points on the surface where the acceleration is evaluated, but it is clear that MASC is not suitable for rectangular shapes since it can not model the edges very well. The MSP has a similar problem with the edges, but the error is smaller compared to MASC. Overall, the PM has in this test case strong advantages over the mascon methods with a neglectable error ($10^{-12}\%$) and the lowest computation time.

Comparison on Phobos

As shown for the cube in the previous section, we consider the PM as the reference solution for the gravitation of the polyhedron shape model of Phobos provided by [21]. For this shape, we have computed the surface gravity using PM in Figure 12. We can see circular and relatively strong gravitation in the -Z-direction and in the +Z-direction (vertical). Also, the lowest gravitation appears to be near the Stickney crater (Figure 12d, 12f).

The *relative* comparison is done taking the ratio τ^{PM} of the resulting gravitation of the two individual mascon methods g_{mascon} to the PM g_{PM} as:

$$\tau^{PM} = \frac{g_{mascon}}{g_{PM}} \cdot 100\% \tag{10}$$

Again, a percentage $\tau^{PM} < 100\%$ represents an under-estimate of the gravity, $\tau^{PM} = 100\%$ is a perfect match, and $\tau^{PM} > 100\%$ represents an over-estimate (over-shoot) of the gravity.

We have generated three different sphere packings with MSP, ranging from 100k to 800k spheres. Also, we can overall observe similar results in Table 5 as in the cube test case. As expected, the mean error is smaller than in the cube test case. Even if we use significantly fewer spheres, the MSP performs better than in the cube case. From Figure 13 we can also observe the noisy pattern and also blueish circular pattern (Figure 13c), that we already know from the cube case. Again, the overshooting pattern comes from the MSP heuristic and the blueish spots indicate a lack of smaller spheres in that area.

Table 5: Phobos: Comparison of gravitation of the two mascon methods compared to the PM.

Method	Min. [%]	Mean [%]	Max. [%]	σ [%]
MSP 100k	98.9972	100.0193	100.9009	0.2577
MSP 400k	99.4752	100.0118	100.5060	0.1473
MSP 800k	99.4878	100.0092	100.4153	0.1122
MASC 64.8k	96.9273	100.1197	104.9161	0.7071

The shape of Phobos is much more suitable for MASC since it is related to an ellipsoidal shape representation. This can be seen by the results of the comparison with PM in Table 5. The mean value of the gravitational acceleration is on the surface in good agreement with the solution by PM. A few points (red in Figure 13) exist showing an overestimation of the acceleration. They are all related to the bottom of craters, i.e. the depth of the bottom of the craters is large enough. Underestimation is related to the rims of the crater, which can be clearly seen at the Stickney crater. It can be concluded that the overall performance of MASC is in very good agreement with results obtained by PM, the small parts with under and over performance can be improved by a higher resolution at the specific locations. Such a variable resolution at specific locations has not been implemented yet, but is planned for the future.

Again, due to the different machines used, we do not report the absolute computation times. However, a strong disadvantage of the PM was the computation time of about 12 hours for the detailed shape model paired with a large (global) number of evaluation points. The computation time for MSP compared to PM was by two orders of magnitude faster than PM. Also, MASC was by one order of magnitude 1 significantly faster than PM.

The largest deviations for the mascons method seem to appear where striking features as craters or terrain elevations appear. For craters, this can be seen well in the Figures 13a (blue spot) and 13d (yellowish circular). In the -Z-view direction smaller craters are more remarkable with MASC than with

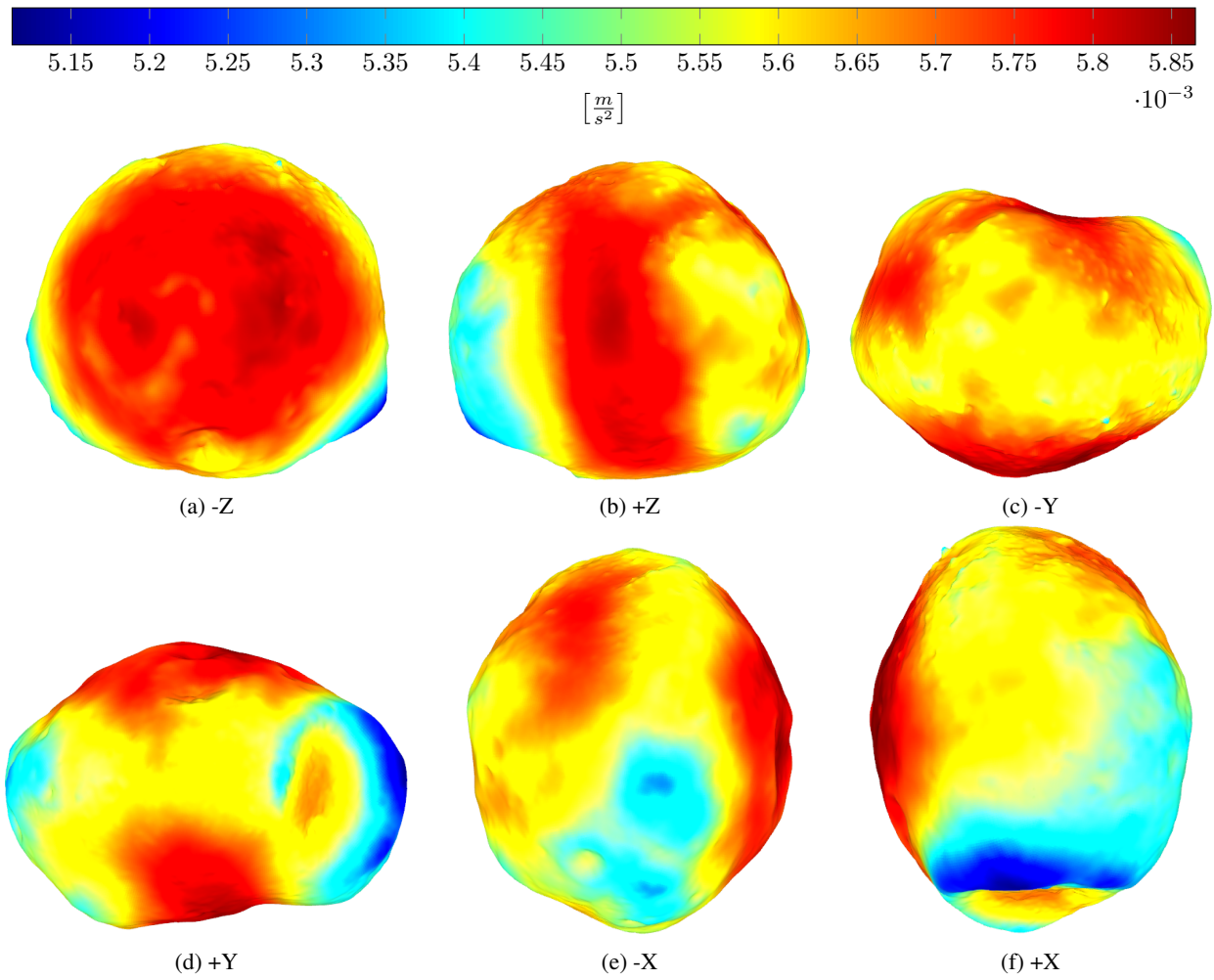

(a) -Z (b) +Z (c) -Y

(d) +Y (e) -X (f) +X

Figure 12: Surface gravity computed with PM for Phobos: min. (blue) and max. (red). Axis indicates the viewing direction. Larger gravitation for $\pm$ Z and smaller for $\pm$ X viewing direction. Also increased gravitation at giant crater Stickney (visible in +Y direction, on the right side).

MSP. Also the elevation around the Stickney crater is visible for both methods (blueish, Figure 13b, 13e). Another two elevations can be seen in the -X-direction and lower part in Figures 13c and 13f. Overall, we can say that the striking features are less outstanding for the MSP 800k than for the MASC 64.8k method.

To summarize: PM gives us the most accurate results for Phobos but has also the highest computation time. The mascon methods both have similar issues with craters and elevations, yet they are more outstanding for MASC. However, this issue might be different with a higher resolution model of Phobos. The lowest computation time has the MSP method with the lowest reported error of 0.0092% on average.

6. Discussion

This work provides a systematic comparison between three different methods to compute gravitational acceleration. In the context of small Solar System body exploration, each method has different advantages and disadvantages, making them more or less suitable for various application cases.

Firstly, assuming that a polyhedral shape file of the small body of interest is available, we have shown that, assuming constant density, we can arrive at a computationally expensive exact solution for the gravity field. This can be useful for early mission planning, but the limitation with respect to inhomogeneities demands future work as will be discussed in the final section. This disadvantage does not appear for the two mascon methods. Moreover, we observed, that the accuracy of the "exact" polygonal method, depends on the polygonal resolution, which is obvious, but, to our knowledge, has never been quantified, but also to the *parametrization* of the shape. This is an important factor that requires further investigation.

Secondly, while computation time is non-crucial as long as the spacecraft is on the ground, it becomes an important aspect during the mission proximity operations in the target. Here, different use cases might demand quick computation time, e.g. when performing large numbers of computations times such as for a Monte Carlo analysis. For example, the JAXA MMX mission will deploy the MMX rover to land on Phobos and both ESA Hera carry-on CubeSats (Juventas and Milian) will/consider to (respectively) attempt landing on Dimorphos. While we identified some (little) uncertainty in

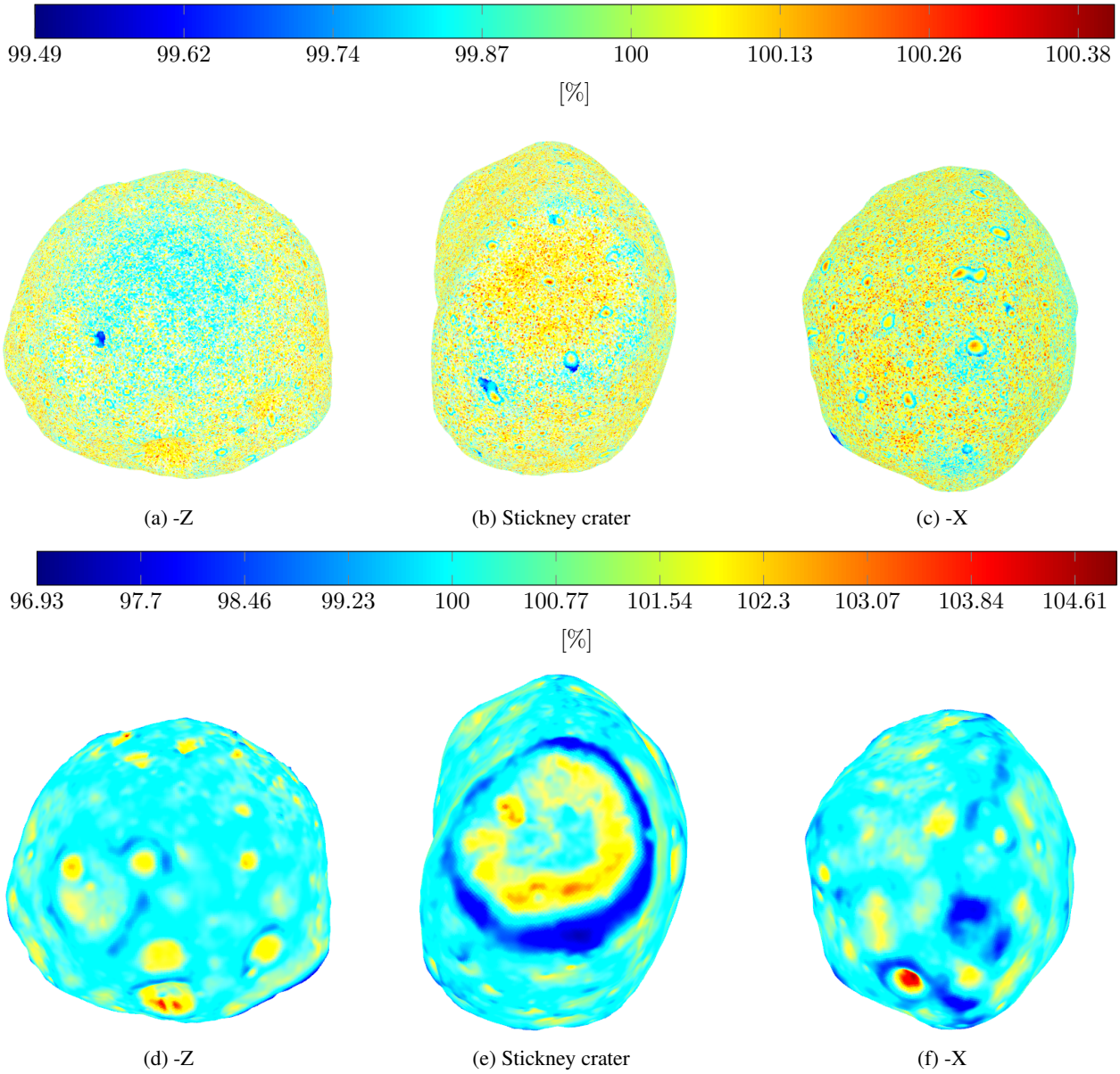

(a) -Z (b) Stickney crater (c) -X

(d) -Z (e) Stickney crater (f) -X

Figure 13: Surface gravity comparison of mascon methods to polygon method as percentage reference: min. (blue) and max. (red). Axis is showing view direction. First row (13a, 13b, 13c) is using MSP 800k and second row (13d, 13e, 13f) MASC with 64.8k mascons.

the exterior gravitation computation in the mascon methods, the computation times will allow a detailed landing analysis where uncertainties in the initial conditions (deployment conditions) can be accounted for a large number of possible descent trajectories (that is integrated using the acting gravity at each integration step). Therefore, the quick methods allow live (online) decision-making for mission operators, or even autonomous decisions onboard a spacecraft, ensuring the best deployment conditions while minimizing the risk of arriving in unsafe landing locations. The same reasoning can be extended to so-called touch-and-go maneuvers, often performed for sample-return missions. Here, we also recall that spherical and elliptical harmonics generally used for mission analysis on-orbit will break down within the Brillouin sphere, making them less usable for close-proximity operations than the three methods tested here.

Third, we consider the surface itself, either stationary landed as the CubeSats Juventas and Milani, or roving such as the DLR/CNES MMX rover. Here, the computation of surface gravity can be useful for data analysis, e.g. of the Juventas surface gravimeter GRASS, but also for rover surface operations, e.g. ensuring good roving stability, minimizing the risk of tipping over. Locally, we found that on the surface the mascon errors can be relatively large, favoring the PM method. However, a hierarchical approach with high resolution on the local scale and lower resolution further away might be favorable, possibly combining different methods.

7. Conclusion and Future Work

In this study, we have at first presented three different methods to compute the gravitational acceleration for irregular-shaped and homogeneous bodies. Our first method (PM) was based on the polyhedral method and our second and third were based on the mascon method. The second method (MSP) uses sphere packings to represent the mascons, whereas our third method (MASC) uses spherical coordinates to subdivide the body into solid elements.

Then, we defined three test cases to provide a solid comparison between our methods and analytical expressions for the gravitational acceleration. In the first test case, we had a sphere that we have approximated with different polygonal meshes (Icosphere, UV sphere). For our second test case, we have created a polygonal model of a cube and in the third test case, we have chosen the Martian innermoon Phobos. For every test case, we have described in detail the parameter settings and also how we have determined our evaluation points.

Overall, our test case setup allowed us to highlight the strength and limits for each method in each case. For the sphere case, the mascons methods can provide the most exact solution. A direct comparison would be trivial. So we compared them by using the polygonal model of the sphere. This allowed us a non-trivial comparison with the mascon methods. PM showed a relatively high computation time with an increased number of facets. From the cube case, we could see, that the polygon method had an advantage over the mascon methods since it provided a solution that was almost equal to the analytical solution. The mascon methods had the largest errors, this was the worst case for them. Also, the advantage for PM was here, that the polygonal cube shape can be exactly described with few faces. However, this changed in our Phobos case, where we have had more faces and complexity. Since no ground truth data is available, we compared our mascon methods to the polygonal method (PM). The MSP method performed better in the Phobos case compared to MASC. It provided higher accuracy and in general fast computation times. With the results of the test cases we conclude, that we presented efficient and accurate methods to compute the gravitational field of irregular-shaped bodies. Their complex gravitational fields are especially important in the physically-based simulation of space missions with guidance, navigation, and control algorithms.

Furthermore, we want to investigate different density distributions. This extension would make them even more applicable for gravitational simulations. Also, this opens a way to verify solutions to the inverse gravitational problem. Another issue, that we want to make more clear, is probably the effect of choosing the location for the evaluation points. Other properties like inertia around the principal axes would also be highly interesting to compare between different methods.

Acknowledgments

M.N. acknowledges funding from the Foundation of German Business (sdw) and the Royal Observatory of Belgium (ROB) PhD grants. The work by Bundeswehr University was carried out in the frame of project KaNaRiA-NaKoRa, financed by the German Ministry of Economy and Energy and administered by the German Aerospace Center, Space Administration (DLR, Deutsches Zentrum für Luft- und Raumfahrt, FKZ 50NA1915). The work on the part of University of Bremen presented in this paper was partially funded by DLR under grant 50NA1916.

References

[1] M. Yoshikawa, J. Kawaguchi, A. Fujiwara, and A. Tsuchiyama, *Hayabusa Sample Return Mission*, 2015, pp. 397–418.

[2] Y. Tsuda, M. Yoshikawa, M. Abe, H. Minamino, and S. Nakazawa, "System design of the Hayabusa 2—Asteroid sample return mission to 1999 JU3," *Acta Astronautica*, vol. 91, pp. 356–362, Oct. 2013.

[3] W. M. Kaula, *Theory of satellite geodesy: applications of satellites to geodesy*. Courier Corporation, 2013.

[4] G. Romain and B. Jean-Pierre, "Ellipsoidal Harmonic expansions of the gravitational potential: Theory and application," *Celestial Mechanics and Dynamical Astronomy*, vol. 79, no. 4, pp. 235–275, Apr. 2001. [Online]. Available: https://doi.org/10.1023/A:1017555515763

[5] R. S. Park, R. A. Werner, and S. Bhaskaran, "Estimating small-body gravity field from shape model and navigation data," *Journal of guidance, control, and dynamics*, vol. 33, no. 1, pp. 212–221, 2010.

[6] R. A. Werner and D. J. Scheeres, "Exterior gravitation of a polyhedron derived and compared with harmonic and mascon gravitation representations of asteroid 4769 castalia," *Celestial Mechanics and Dynamical Astronomy*, vol. 65, no. 3, pp. 313–344, 1996.

[7] Y. Takahashi and D. Scheeres, "Morphology driven density distribution estimation for small bodies," *Icarus*, vol. 233, pp. 179–193, 2014.

[8] M. Noeker, Ö. Karatekin, B. Ritter, and E. Tasev, "Artificial terrain on Phobos: Assessing the influence on local gravity using the Wedge-Pentahedra Method," in *Copernicus Meetings*, vol. 2021, no. EPSC2021-370.

[9] S. Le Maistre, A. Rivoldini, and P. Rosenblatt, "Signature of Phobos' interior structure in its gravity field and libration," *Icarus*, vol. 321, pp. 272–290, 2019.

[10] A. Srinivas, R. Weller, and G. Zachmann, "Fast and accurate simulation of gravitational field of irregular-shaped bodies using polydisperse sphere packings." in *ICAT-EGVE*, 2017, pp. 213–220.

[11] W. Yin, L. Shu, Y. Yu, and Y. Gao, "Use of tetrahedral finite element method for computing the gravitation of irregular-shaped asteroid," *IOP Conference Series: Materials Science and Engineering*, 2019.

[12] M. E. Mostafa, "Modelling magnetic anomalies of solid and fractal bodies with defined boundaries using the finite cube elements method," *Geophysical Journal International*, vol. 177, no. 1, pp. 62–70, 2009.

[13] B. Ritter, Ö. Karatekin, M. van Ruymbeke, M. Noeker, E. Ümit, R. Laguerre, S. Berkenbosch, S. Bonnewijn, E. van Ransbeeck, E. Neefs *et al.*, "GRASS: a Gravimeter for the Investigation of Small Solar System Bodies," in *EPSC-DPS Joint Meeting 2019*.

[14] M. Noeker, E. Van Ransbeeck, Ö. Karatekin, and B. Ritter, "Development of a compact payload mechanism enabling continuous motorized sensor head rotation and signal transfer," in *ESMATS 2021*, vol. 19, no. 18, 2021.

[15] Ö. Karatekin, B. Ritter, J. Carrasco, M. Noeker, E. Umit, E. Vanransbeeck, H. Alaves, E. Tasev, M. Goli, H. Gold-

berg *et al.*, "Surface gravimetry on Dimorphos," in *EGU General Assembly Conference Abstracts*, 2021, pp. EGU21–15 901.

[16] M. Vayugundla, T. Bodenmüller, M. J. Schuster, M. G. Müller, L. Meyer, P. Kenny, F. Schuler, M. Bihler, W. Stürzl, B.-M. Steinmetz, J. Langwald, A. Lund, R. Giubilato, A. Wedler, R. Triebel, M. Smíšek, and M. Grebenstein, "The MMX Rover on Phobos: The Preliminary Design of the DLR Autonomous Navigation Experiment," in *2021 IEEE Aerospace Conference (50100)*, 2021, pp. 1–18.

[17] Y. Kawakatsu, K. Kuramoto, T. Usui, H. Ikeda, N. Ozaki, N. Baresi, G. Ono, T. Imada, T. Shimada, H. Kusano *et al.*, "Mission Design of Martian Moons eXploration (MMX)," in *69th International Astronautical Congress*, 2018.

[18] E. Tasev, "Determination of the interior structure of small bodies of the Solar System," pp. 1–53, 2019.

[19] S. Van wal, "High-fidelity simulation of small-body lander/rover spacecraft," Ph.D. dissertation, University of Colorado Boulder, 2018.

[20] R. Weller and G. Zachmann, "Protosphere: A gpu-assisted prototype guided sphere packing algorithm for arbitrary objects," in *ACM SIGGRAPH ASIA 2010 Sketches*, ser. SA '10. New York, NY, USA: Association for Computing Machinery, 2010. [Online]. Available: https://doi.org/10.1145/1899950.1899958

[21] K. Willner, X. Shi, and J. Oberst, "Phobos' shape and topography models," *Planetary and Space Science*, vol. 102, pp. 51–59, 2014.

[22] S. Tardivel, "The limits of the mascons approximation of the homogeneous polyhedron," 09 2016.

[23] M. Pätzold, T. P. Andert, G. L. Tyler, S. W. Asmar, B. Häusler, and S. Tellmann, "Phobos mass determination from the very close flyby of Mars Express in 2010," *Icarus*, vol. 229, pp. 92–98, Feb. 2014. [Online]. Available: https://ui.adsabs.harvard.edu/abs/2014Icar..229...92P

[24] M. Pätzold, T. Andert, M. Hahn, S. W. Asmar, J. P. Barriot, M. K. Bird, B. Häusler, K. Peter, S. Tellmann, E. Grün, P. R. Weissman, H. Sierks, L. Jorda, R. Gaskell, F. Preusker, and F. Scholten, "A homogeneous nucleus for comet 67P/Churyumov-Gerasimenko from its gravity field," *Nature*, vol. 530, pp. 63–65, Feb. 2016. [Online]. Available: https://ui.adsabs.harvard.edu/abs/2016Natur.530...63P

[25] C. H. Acton, "Ancillary data services of NASA's Navigation and Ancillary Information Facility," *Planetary and Space Science*, vol. 44, no. 1, pp. 65–70, Jan. 1996. [Online]. Available: https://linkinghub.elsevier.com/retrieve/pii/0032063395001077

[26] X. Li and M. Chouteau, "Three-dimensional gravity modeling in all space," *Surveys in Geophysics*, vol. 19, no. 4, pp. 339–368, 1998.

[27] M. Okabe, "Analytical expressions for gravity anomalies due to homogeneous polyhedral bodies and translations into magnetic anomalies," *Geophysics*, vol. 44, no. 4, pp. 730–741, 04 1979. [Online]. Available: https://doi.org/10.1190/1.1440973

[28] O. Witasse, T. Duxbury, A. Chicarro, N. Altobelli, T. Andert, A. Aronica, S. Barabash, J. L. Bertaux, J. P. Bibring, A. Cardesin-Moinelo, A. Cichetti, V. Companys, V. Dehant, M. Denis, V. Formisano, Y. Futaana, M. Giuranna, B. Gondet, D. Heather, H. Hoffmann, M. Holmström, N. Manaud, P. Martin, K. D. Matz, F. Montmessin, T. Morley, M. Mueller, G. Neukum, J. Oberst, R. Orosei, M. Pätzold, G. Picardi, R. Pischel, J. J. Plaut, A. Reberac, P. Pardo Voss, T. Roatsch, P. Rosenblatt, S. Remus, N. Schmedemann, K. Willner, and T. Zegers, "Mars Express investigations of Phobos and Deimos," *Planetary and Space Science*, vol. 102, pp. 18–34, Nov. 2014. [Online]. Available: https://ui.adsabs.harvard.edu/abs/2014P&SS..102...18W

BIOGRAPHY

Hermann Meißenhelter *received his B.S. and M.S. in computer science from University of Bremen. He joined the institute Computer Graphics and Virtual Reality at the University of Bremen in 2019. Currently, he works as a research associate at that institute. His scientific interests are packing problems and collision detection.*

Matthias Noeker *received his M.Sc. degree in Aerospace Engineering (TU Delft) in 2018, his B.Sc. degree in Mechanical Engineering (University of Siegen) in 2016, and his BEng degree in Mechanical and Manufacturing Engineering (University of Portsmouth) in 2015. He is currently a PhD candidate at the Royal Observatory of Belgium and at UCLouvain, working on the GRASS gravimeter development and gravity modelling.*

Tom Andert *received his diploma in 2004 and his Ph.D. in 2010 in Geophysics from the University of Cologne, Germany. He is currently a senior researcher and leads the Radio Science research group at the Institute of Space Technology and Space Applications (ISTA) at the Bundeswehr University in Munich. His scientific interests include among others measuring and interpreting the gravity field of small solar system bodies using radio science data from interplanetary missions.*

René Weller *is a postdoctoral research assistant at the Computer Graphics Group at the University of Bremen, where he also received his Ph.D. degree in computer science in 2012. He is working in the field of computer graphics and virtual reality with a specialization in collision detection algorithms.*

Benjamin Haser *received his B.S. and M.S degrees in physics from Ludwig-Maximilians-University Munich in 2019. He is currently a research associate and Ph.D. student at Universität der Bundeswehr München, taking a leading role at the AI group at ISTA. He focusses on AI methods for space applications, especially Machine Learning, Deep Learning, Reinforcement Learning and Genetic and Evolutionary Algorithms.*

Özgür Karatekin *has obtained his Ph.D in Applied Sciences, from Université Libre de Bruxelles and von Karman Institute for Fluid Dynamics, Brussels Belgium. His main scientific expertise lies in the planetary geophysics, and in particular in rotation, gravity and tidal interactions. He has been involved with several ESA/NASA planetary missions, at PI and co-I level. He is the leading scientist (PI) on the GRASS instrument.*

Birgit Ritter *received her Ph.D degrees in Physics from CAU Kiel in cooperation with DLR Cologne, Germany, in 2013. She is project and instrument manager and experimental scientist for the gravimeter for small Solar System bodies (GRASS) instrument development.*

Max Hofacker *received his B.S and M.S degrees in Geodesy and Geoinformation from TUM where he specialized in satellite navigation and earth sciences. Currently he is working at UniBW as PhD-candidate researching satellite landing emulation techniques.*

Larissa Balestrero Machado *received her B.Sc. and M.Sc. degrees in Aerospace Engineering from Florida Institute of Technology in Melbourne, Florida. She joined the Bundeswehr University Munich in 2019 as a researcher and PhD candidate. Larissa's main research topics include GNC systems for autonomous landing on small planetary bodies and space systems design.*

Gabriel Zachmann *is a full professor with the computer science department at the University of Bremen, Germany. He is the head of the visual computing group, focusing mostly on computer graphics and virtual reality. Prior to that, he was a professor for 7 years at the Technical University of Clausthal, Germany, where he established a research group for computer graphics. He has worked in virtual reality, geometric computing, and visual computing in general for 25 years.*